Water Research X 19 (2023) 100185

Contents lists available at ScienceDirect

Water Research X

journal homepage: www.sciencedirect.com/journal/water-research-x

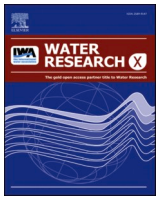

Mechanism insight into the facet-dependent photoaging of polystyrene microplastics on hematite in freshwater

Jiehong He [a], Lanfang Han [a,*], Weiwei Ma [a], Chao Xu [b], Elvis Genbo Xu [c], Chuanxin Ma [a], Baoshan Xing [d], Zhifeng Yang [a]

[a] Key Laboratory for City Cluster Environmental Safety and Green Development of the Ministry of Education, School of Ecology, Environment and Resources, Guangdong University of Technology, Guangzhou 510006, PR China
[b] Research Center for Eco-Environmental Engineering, Dongguan University of Technology, Dongguan 523808, PR China
[c] Department of Biology, University of Southern Denmark, Odense 5230, Denmark
[d] Stockbridge School of Agriculture, University of Massachusetts, Amherst, MA 01003, USA

ARTICLE INFO

Keywords:
Microplastics
Photodegradation
Hematite
Crystal facets
Reactive oxygen species

ABSTRACT

Hematite, as an extensive natural mineral with multiple crystal facets, profoundly affects the migration and transformation of pollutants in the natural environment. However, little is known about the photochemical behavior of microplastics on different facets of hematite in the aquatic environment. In this work, the photoaging of polystyrene microplastics (PS-MPs) on different crystal planes ({001}, {100}, and {012} facets) and related mechanisms were studied. Two-dimensional correlation spectroscopy analysis illustrated that the reaction pathways of PS-MPs photoaging on hematite tended to preferential chemical oxidization. The stronger performance of PS-MPs photoaging, expressed by particle size reduction and surface oxidation, was observed on the {012} crystal facet. Under irradiation, {012} facet-dominated hematite with a narrower bandgap (1.93 eV) reinforced the photogenerated charge carrier separation, and the lower activation energy barrier (1.41 eV calculated from density functional theory) led to effective •OH formation from water oxidation. These findings elucidate the underlying photoaging mechanism of MPs on hematite with different mineralogical phases.

1. Introduction

Microplastics (MPs, size $\leq$ 5 mm) have become emerging pollutants and attracted worldwide attention (Nguyen et al., 2019; Tang et al., 2021). Due to the small sizes, most MPs cannot be intercepted with sewage treatment and are therefore released into freshwater (Novotna et al., 2019). It has been estimated that 80% of MPs in surface water come from sewage treatment (Parashar and Hait, 2022). As a significant sink for pollutants, freshwater ecosystems have been contaminated by MPs (e.g., Taihu, 3.4–25.8 items/L and Poyang Lake, 5–34 items/L in China;) (Hu et al., 2020; Minor et al., 2020; Su et al., 2016; Yuan et al., 2019). While studies are accumulating reporting the MPs occurrence in freshwater, the understanding of environmental behavior (e.g., transformation, degradation, and bioaccumulation) of MPs in realistic freshwater is limited, which holds importance in assessing the comprehensive ecological and health risks associated with MPs.

Photoaging is considered a principal process of MPs transformation (Mao et al., 2020; Zhang et al., 2022a), which is affected by the coexisting components in freshwater (e.g., organic matter, inorganic salts, and minerals). For instance, dissolved organic matter (DOM) (e.g., fulvic acid, humic acid, etc.) can exhibit promotional or hindering effects on MPs photoaging (Wu et al., 2021; Zhang et al., 2022b). Zhu et al. (2022) explored the effect of inorganic ions (e.g., NO_3^-, HCO_3^-, etc.) on PS-MPs photoaging. However, little is known about the mediating role of minerals on MPs photoaging, although plentiful studies have highlighted the significant impacts of minerals on the fate of environmental pollutants (Ma et al., 2020; Zhou et al., 2012).

Among various widespread minerals, hematite (α-Fe_2O_3) shows a wide visible-light absorption capacity (Shen et al., 2016) and has been used as a natural photocatalyst for pollutant degradation (Asif et al., 2021). It exhibits vast morphological properties with the exposure of facets possessing distinct structures and properties (Cornell and Schwertmann, 2003), thereby impacting ROS formation (Cornell and Schwertmann, 2003; Lv et al., 2010). Hematite {012} is reported to possess more surface hydroxyl groups than hematite {100} (Qiu et al., 2022), which could impact ROS production (Yu et al., 2019). Thus, we

* Corresponding author.
E-mail address: hanlanfang@gdut.edu.cn (L. Han).

https://doi.org/10.1016/j.wroa.2023.100185
Received 16 April 2023; Received in revised form 17 May 2023; Accepted 26 May 2023
Available online 27 May 2023

hypothesize that (1) the photochemical activity of hematite differs based on the structure and surface properties of distinct facets; and (2) the dominant facet determines the activation barrier for ROS generation, thus modulating MPs photoaging.

The overarching objective of this study is to reveal the mediating role of hematite facets in PS-MPs photoaging, the most common MPs in freshwater (Lithner et al., 2011; Liu et al., 2019). Specifically, this study aims to (1) probe the effects of facets of hematite on the photoaging behavior of PS-MPs; (2) unravel the variability of ROS generation on different facets; and (3) inquire into the structural alterations and molecular characteristics during the PS-MPs photoaging. The findings contribute to an in-depth understanding of the effects and mechanisms of the crystallographic surface structures of hematite on the photoaging process of PS-MPs in freshwater.

2. Results and discussion

2.1. Structural characteristics of hematite with different facets

The XRD showed the distinct crystal structure of hematite (JCPDS No. 33-0664) (Fig. S1a), and the structural unit cells of each crystal plane based on DFT simulations were provided in Fig. S1b and c. The sharp peaks indicated good crystallinity of α-Fe_2O_3. All samples represented the adsorption isotherms of type IV and H3 hysteresis loops (Fig. S2a and b). 012FeC revealed higher S_{BET} (35.44 m^2/g) than 001FeH (28.92 m^2/g) and 100FeR (10.85 m^2/g) (Table S2) with more abundant mesoporous structures (Bardestani et al., 2019; Li et al., 2017).

From the FESEM analysis, 001FeH, 100FeR, and 012FeC showed regular morphologies with hexagonal nanoplates, nanorods, and nanocubes, respectively (Fig. 1a–c, the geometric models inserted into the higher right corner). TEM images further demonstrated the structure (Fig. 1d–f). Specifically, 001FeH displayed the geometric model of nanoplates with the length of ~233 nm and the thickness of ~10 nm. Nanorods were observed on 100FeR with a length of ~183 nm and a radius of ~43 nm, and 012FeC showed the shape of nanocubes with a length of ~40 nm. HRTEM and selected area electron diffraction (SAED) were performed to investigate the crystal orientation and crystallinity. The lattice distance of 001FeH was 0.25 nm with the angle of the two adjacent facets at 117° (Fig. 1g). The diffraction spots with hexagonal symmetry presented in the SAED pattern indicated that the bottom/top surfaces were bound by {001} facets. For 100FeR, the measurable lattice spacing in the top surface was 0.25 nm, corresponding to {110} lattice planes (Fig. 1h). The SAED pattern (inserted in Fig. 1h) displayed a single crystalline structure and implied {110}, {113}, and {013} lattice spots. According to a previous study (Lv et al., 2018), the side surfaces of the nanorods (100FeR) might be ascribed to the {100} and equivalent lattice planes. As for 012FeC, the HRTEM images showed a lattice spacing of 0.37 nm assigned to the {012} facets and an interfacial angle of 90° (Fig. 1i). Combined with the structural features of the single crystal in SAED (inserted in Fig. 1i), the main facets of 012FeC could be indexed to {012} facets.

The surface electronic properties of all samples were probed by XPS. Fe2p3/2 and Fe2p1/2 peaks were located at approximately 710.5 and 724.1 eV, respectively, and additional satellite peaks were observed at 718.7 and 732.5 eV. Similar peak areas at Fe2p indicated similar Fe(III) content in all samples (Fig. S2c) (Qiu et al., 2022). In the O1s region, the lowest peak at approximately 529.4 eV could be assigned to lattice oxygen in the α-Fe_2O_3 (Fe-O) (Fig. S2d). The peaks at approximately 531.0 eV, 532.1 eV, and 533.5 eV were assigned to lattice hydroxyl groups (Fe-OH lattice), hydroxyl groups (Fe-OH adsorbed), and water on the surface (Baltrusaitis et al., 2007). The content of different species in the

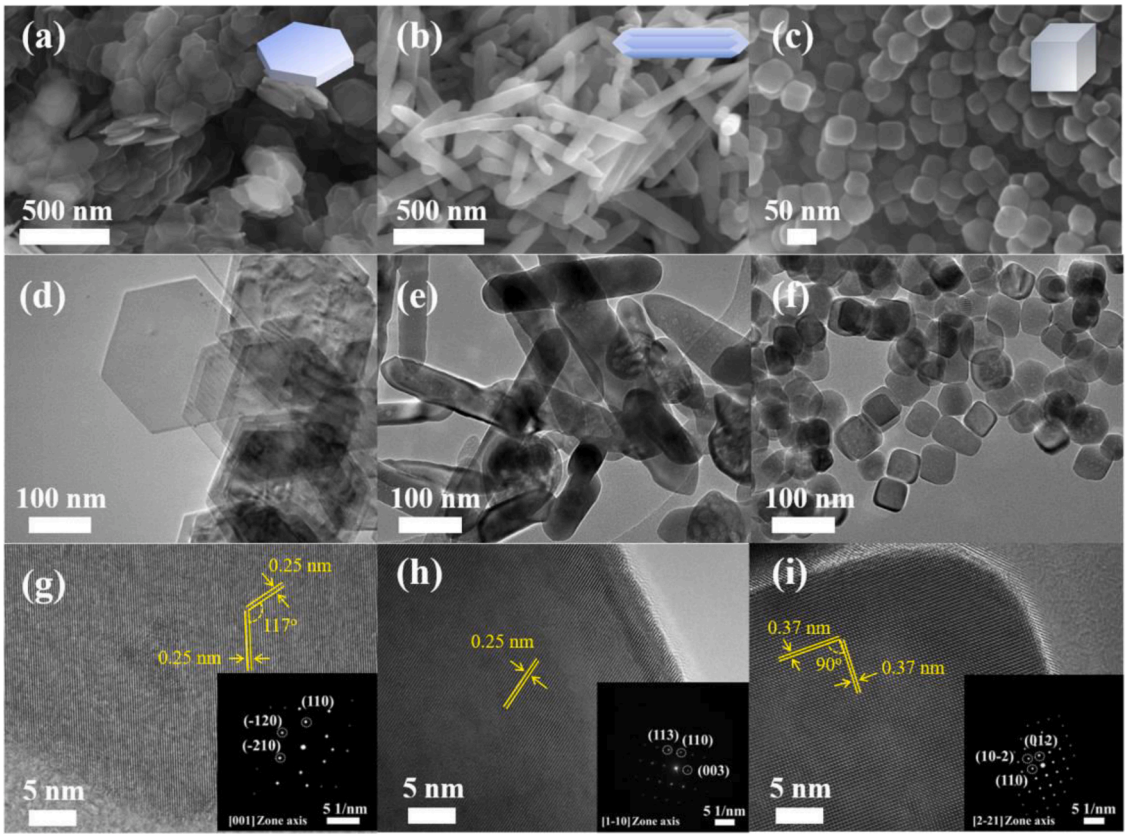

Fig. 1. Scanning electron microscope (SEM) images of hematite exposed with {001} (a), {100} (b) and {012} facets (c). The corresponding geometric models are inserted in the top right corner; transmission electron microscopy (TEM) and high-resolution transmission electron microscopy (HRTEM) images of hematite exposed with {001} (d, g), {100} (e, h) and {012} facets (f, i) with selected area electron diffraction (SAED) in the inset.

O1s spectrum was calculated in Table 1. 012FeC revealed more surface hydroxyl groups (16.2%) than 001FeH (9.9%) and 100FeR (11.6%).

UV-DRS was applied to investigate the light absorption of hematite (Fig. 2a), and the bandgap energy was also calculated from the Tauc plot. All samples exhibited good absorbance of ultraviolet and visible light. 012FeC displayed stronger light absorption in the UV region with a slightly narrower bandgap (1.93 eV) compared to 001FeH (1.99 eV) and 100FeR (1.96 eV). In addition, PL patterns of all samples with an excitation wavelength of 350 nm revealed emission peaks at approximately 440 nm (Fig. 2b). The lower intensity of emission peak on 012FeC indicated lower charge carriers' recombination. Furthermore, the photocurrent spectra revealed a higher electron density on 012FeC than 001FeH and 100FeR (Fig. 2c). EIS analysis revealed a smaller arc radius obtained on 012FeC, corresponding to a smaller impedance and faster migration of carriers (Fig. 2d). In general, the photochemistry property of hematite samples with different crystalline facets differed, and 012FeC exhibited lower photogenerated charge carriers' recombination, higher photoelectron density and the faster migration of carrier.

2.2. Particle size and functional groups of photoaged PS-MPs on hematite

PS-MPs photoaging on hematite with different facets was investigated under full wavelength irradiation. Hematite adsorption under dark condition was conducted for comparison. It showed that only ~10 wt% of the hematite were adsorbed and almost no change of PS-MPs was found (Fig. S3), indicating the negligible contribution of sorbed hematite to the particle size reduction. It was also found no almost particle size reduction in dark control without hematite, indicating the negligible effect of stirring on particle size reduction of PS-MPs. However, under irradiation, all aged PS-MPs displayed the decreased particle size (Fig. 3a), and enhanced particle size reduction was observed with hematite addition compared to the pure photolysis (12.3%). Specifically, 012FeC displayed the highest particle size reduction (52.8%) compared to 001FeH (20.0%) and 100FeR (39.1%) after 12 h of irradiation. Pseudo-first-order kinetics was adopted and the kinetic constants (k) calculation revealed a faster reduction rate (0.053) on 012FeC than 001FeH (0.019) and 100FeR (0.037) (Fig. 3b). These results indicated that hematite, especially 012FeC, could effectively promote particle size reduction of PS-MPs during irradiation.

The alterations of functional groups of aged PS-MPs were also probed by FTIR (Fig. S4), which could effectively evaluate the oxidation of PS-MPs during photoaging (Duan et al., 2022). Prominent bands at 2851, 1600, 1452, 756, and 698 cm^{-1} were observed for pristine PS-MPs, and the assignments were summarized in Table S2. All aged PS-MPs displayed intense C=O bands at 1742 cm^{-1}, indicating more oxygen-containing group formation. The ratio of the C=O band to the symmetric stretching band of CH_2 at 1452 cm^{-1}, i.e., the carbonyl index (CI), was adopted to evaluate the surface oxidation of PS-MPs (Dong et al., 2022). Fig. 3c shows that no alteration in dark control and increased CI values in light irradiation. It reached the highest on 012FeC (0.68) after 12 h irradiation, which was 3.6 times greater than photolysis (0.19). In general, hematite with different facets promoted the PS-MPs photoaging, with {012} facet exhibiting the strongest promotion of size reduction and surface oxidation.

Further investigation of the functional group was provided by the XPS of pristine and aged PS-MPs (Fig. 3d). From the C1s spectra, four peaks around 284.7, 285.4, 289.1, and 291.1 eV were observed, assigning to C-H, C-O, C=O, and π-π* in PS (Bai et al., 2022). The content of oxygen-containing functional groups (C-O, C=O) in all aged PS increased, especially in the presence of hematite dominated with {012} facets, indicating the surface oxidation of PS-MPs. Small oxidized functional groups in virgin PS-MPs were also observed. This was ascribed to the partial oxidation of PS surfaces during the production or/and crushing process (Dong et al., 2022). In addition, the oxygen-to-carbon atom ratio (O/C) of pristine PS (0.293) increased to 0.398, 0.439, 0.636, and 0.491 in ultrapure water, {001}, {012}, and {100} facets, respectively. This result indicated that the hematite, especially {012} facets-dominated hematite, could accelerate the chemical oxidation of PS-MPs in irradiation, which was consistent with FTIR analysis results.

Table 1
The assignments of the peaks and the content of different species in the O1s spectrum.

Assigned species	001FeH		100FeR		012FeC	
	BE (eV)	Content (%)	BE (eV)	Content (%)	BE (eV)	Content (%)
Fe-O	529.5	71.01	529.5	66.18	529.4	63.04
Fe-OH lattice	531.1	12.82	531.0	15.09	531.0	11.64
Fe-OH adsorbed	532.1	9.850	532.0	11.55	532.2	16.19
H_2O	533.4	6.320	533.4	7.170	533.5	9.140

Note that BE presents binding energy, 001FeH, 100FeR and 012FeC are short for hematite with {001}, {100} and {012} crystal facets, respectively.

2.3. 2D-COS analysis of photoaged PS-MPs and identification of the released DOM

One-dimensional FTIR analysis lacks information on dynamic photoaging and cannot determine the order of functional group variation during PS-MPs photoaging (Zhou et al., 2017). To determine the sequence of functional group changes, two-dimensional correlation spectroscopy (2D-COS) analysis was applied based on one-dimensional FTIR spectral data. The synchronous map showed seven auto-peaks along the diagonal line at 698, 756, 1030, 1493, 1600, 1666, and 1744 cm^{-1} (Fig. 4a). Positive signs for these peaks were observed in all groups after irradiation, implying that all cross-peaks were synchronized with the aging process (Jin et al., 2018). The asynchronous maps were obtained based on Noda's rules, which revealed the sequential order in PS-MPs photoaging (Ding et al., 2020). As shown in Fig. 4b and Table 2, without hematite participation, the chemical bonds of PS-MPs followed the sequential order of 1493 (C=C) > 756 (C-H) > 1600 (C=C) > 1030 (C-O) > 698 (C-H) > 1744 (O-C=O) > 1666 (C=O) under irradiation. However, with 012FeC treatment, the order was 1744 (O-C=O) > 1666 (C=O) > 1030 (C-O) > 1600 (C=C) > 756 (C-H) > 1493 (C=C) > 698 (C-H). Similar results were found on {100} and {001} facets. It was found that carbonyl groups were formed rapidly with the presence of hematite, which might be ascribed to the rapid ROS formation with hematite, accelerating the PS-MPs photoaging and leading to the carbonyl groups formation. Meanwhile, with the presence of hematite, especially {012} facet, the TOC in the solution was higher than photolysis, further indicating the promoting effect of hematite on PS-MPs photoaging. Decreased TOC in the late period was ascribed to the organic's mineralization (Fig. S5a). Additionally, the aromatic structure in the solution was contributed by the monomers from PS-MPs depolymerization and some aromatic intermediate (Fig. S5b). This further indicated that enhanced effect of hematite on PS-MPs photoaging, and the reactivity of various facets differed, which could be correlated with ROS formation on the surface.

2.4. Principal mechanisms revealed by ROS analysis and DFT calculations

To further explore the relationship between the possible reaction path and ROS formation on the different facets, EPR spin-trapping experiments were performed. No signals were observed in the dark control and with no presence of hematite (Fig. 5a). In contrast, the signals of •OH and $^1O_2$ were detected for 012FeC (Fig. 5b and c), suggesting that photogenerated carriers could induce ROS formation by energy transfer or reaction with O_2 and H_2O. It was previously reported that •OH

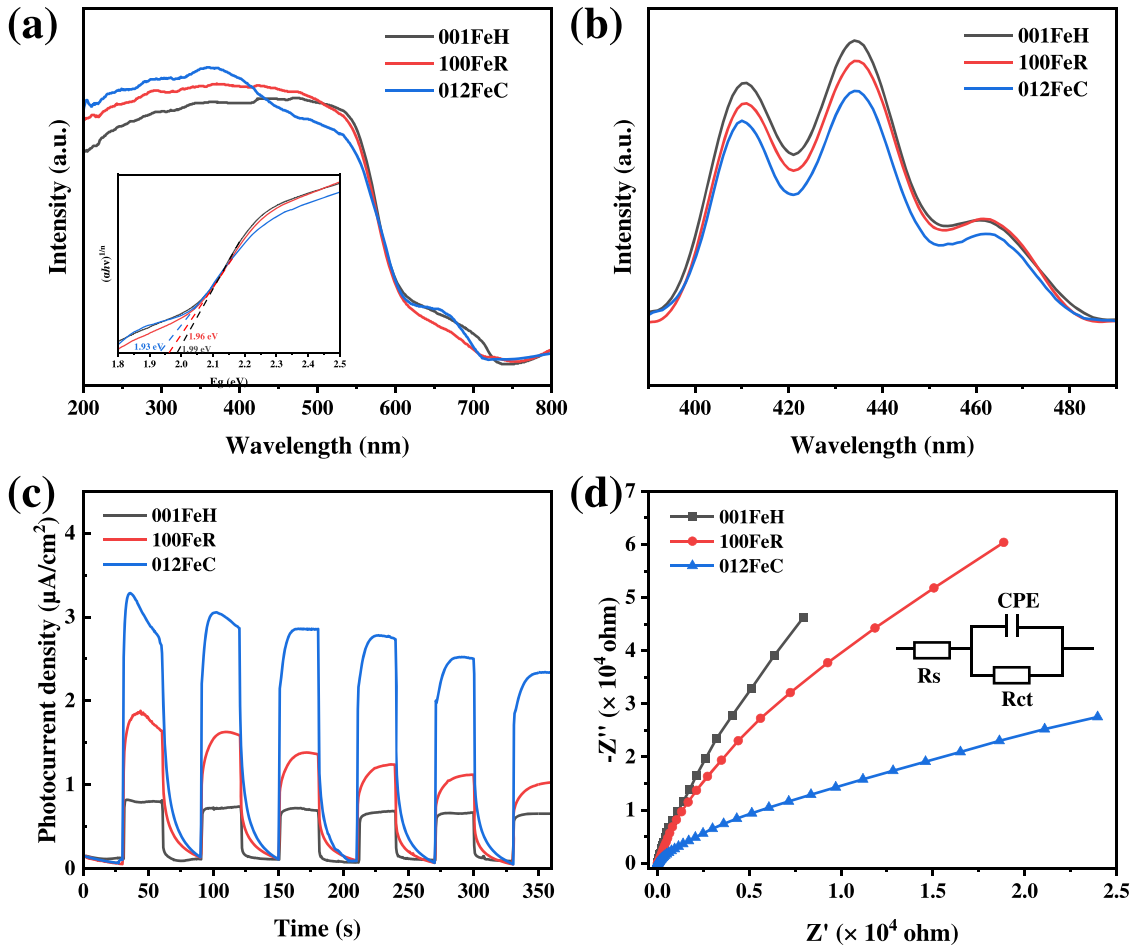

Fig. 2. UV–vis diffuse reflection spectra (UV–vis DRS) of hematite dominated by different crystal facets with the corresponding Tauc plots in the inset (a); steady-state fluorescence spectra at an excitation wavelength of 350 nm (b); photocurrent response spectra under irradiation by a 300 W Xe lamp (c); electrochemical impedance analysis with the equivalent circuit diagram in the inset (d). CPE: constant phase element; Rs: diffusion electric resistance; Rct: charge transfer resistance. 001FeH, 100FeR and 012FeC are short for hematite with {001}, {100} and {012} crystal facets, respectively.

formation could be conducted through the water oxidation or the deformation of $\bullet O_2^-$ (Hussain et al., 2022; Luo et al., 2020). Water oxidation was more possible since the standard potential (2.34 V, $H_2O + h^+_{VB} \rightarrow \bullet OH + H^+$) is more positive than the valence band of hematite (Chen et al., 2021; Zhu et al., 2020). However, the signal of $\bullet O_2^-$ was hardly observed (Fig. S7d–f), which can be ascribed to the conduction band potential of α-Fe_2O_3 was not sufficient for $\bullet O_2^-$ formation (−0.33 V, $O_2 + e^- \rightarrow \bullet O_2^-$) (Chen et al., 2021) (Fig. S6). In addition, the intensity of •OH on different facets was compared (Fig. S7a–c), and the •OH amount was also quantified (Fig. S8). The steady-state concentration of •OH on {012} facets (117.9 uM) was higher than that on {001} (103.2 uM) and {100} (107.8 uM) facets after 70 min irradiation. This was attributed to the lower activation energy barrier (1.41 eV from the DFT calculation below) of {012} facet-dominated hematite, which reinforces •OH formation from water oxidation. Meanwhile, sufficient surface hydroxyl groups (16.2% from XPS analysis) may provide more active sites for PS-MPs photoaging (Qiu et al., 2022). The radical quenching experiment further confirmed the dominant role of •OH (Fig. 5d). The particle size reduction of PS-MPs on 012FeC decreased by ~54.0% after quenching •OH, and it was also inhibited after eliminating photogenerated holes and electrons, suggesting charge carriers in hematite could induce ROS generation.

Overall, our results showed that •OH was the dominant ROS in PS-MPs photoaging. Considering various surface properties and photochemistry properties on different facets, the energy barriers of water oxidation may affect •OH generation. DFT calculations were further conducted to gain insight into the mechanism of water oxidation on different facets. Models of crystal cells and water oxidation configurations in different reaction states are shown in Fig. 6. A transition state (TS) occurred in the reaction of $H_2O^* \rightarrow H^* + OH^*$ at different facets ("*" represented the adsorption site). The activation energy of TS on Fe_2O_3{012} (1.41 eV) was significantly lower than that on Fe_2O_3{100} (4.02 eV) and Fe_2O_3{001} (3.19 eV), benefiting the *OH formation and thereby facilitating the •OH generation. Combining with the analysis of EPR and ROS quantitation, it was inferred that •OH was more easily produced on {012} facet, accelerating PS-MPs photoaging. These theoretical calculations revealed that the surface atomic arrangement of iron oxides determined the activation energy barrier of the water oxidation reaction and therefore affected the efficiency of ROS generation.

3. Conclusions

Reactions on the surface/interface of minerals essentially occur at the exposed facets outside the bulk phase of mineral (Liu et al., 2021). The atomic topology and physicochemical properties of different facets influence the fate of pollutants such as MPs (Yanina Svetlana and Rosso Kevin, 2008). Elucidating the facets effect of minerals on MPs photoaging has important environmental and geochemical implications. In this work, hematite dominated by {001}, {100}, and {012} facets were prepared and applied in PS-MPs photoaging. The structural and photochemical property investigation illustrated that hematite with {012} crystal plane was endowed with faster charge separation and higher

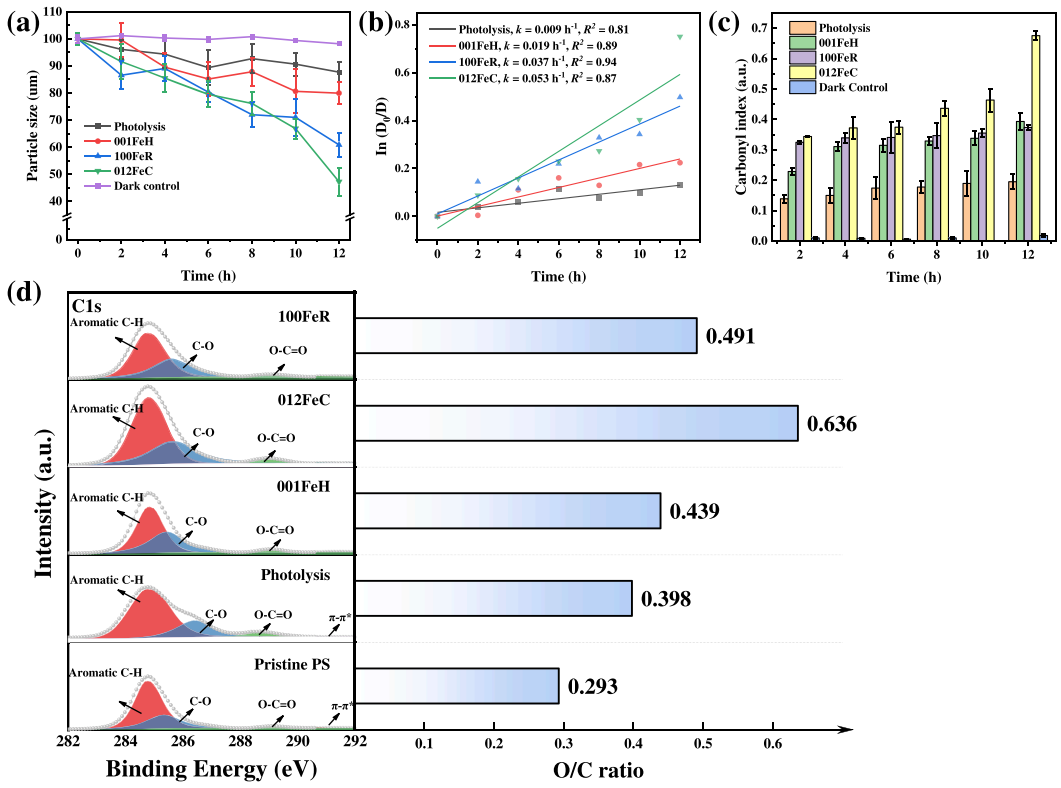

Fig. 3. The particle size (a) and corresponding $\ln(D_0/D)$-time plot (b), carbonyl index (c) of polystyrene microplastics (PS-MPs) on hematite with different crystal facets under irradiation. The C1s spectra and the O/C ratio of pristine and aged PS-MPs after 12 h irradiation from the X-ray photoelectron spectroscopy (d). Note that 001FeH, 100FeR and 012FeC are short for hematite with {001}, {100} and {012} crystal facets, respectively. Dark control represented the reaction in dark condition.

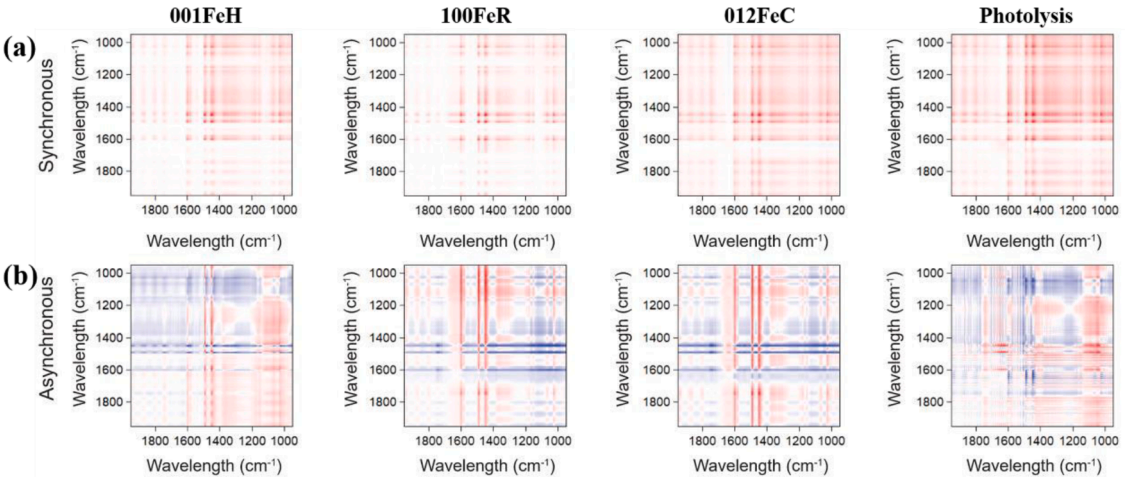

Fig. 4. Two-dimensional correlation spectroscopy (2D-COS) of polystyrene microplastics (PS-MPs) under different irradiation times with pure photolysis, 001FeH, 100FeR and 012FeC, which are divided into synchronous spectra (a) and asynchronous spectra (b). Note that 001FeH, 100FeR and 012FeC are short for hematite with {001}, {100} and {012} crystal facets, respectively.

electron density, which effectively promoted ROS generation, especially •OH. Meanwhile, according to DFT calculations, •OH production was dependent on the activation energy barrier of the exposed facets, and {012} facets were found to have a lower activation energy barrier for water oxidation to •OH. These factors, including the photochemical property of hematite and the activation energy barrier of ROS formation, led to enhanced PS-MPs photoaging, mainly in the form of particle size reduction and elevated surface oxygen-containing groups. Combined with the 2D-COS analysis, the photoaging route of PS-MPs tended to preferential surface oxidization on hematite. This work has disclosed the key features of ROS formation and the mechanism of PS-MPs photoaging on different crystalline hematite, which can help to elucidate the correlation between crystal face mineral characteristics and ROS generation and enrich the molecular basis of PS-MPs photoaging in the presence of hematite with different crystal planes.

Table 2
Two-dimensional correlation spectroscopy (2D-COS) data on the assignment and sign of each cross-peak in synchronous (φ) and asynchronous (ψ, in brackets) maps of polystyrene microplastics (PS-MPs) at 001FeH, 012FeC, 100FeR, photolysis with increasing age time.

Peak (cm^{-1})	Group	Sign						
		698	756	1030	1493	1600	1666	1744
698	C-H	++++	++++ (——)	++++ (-+-)	++++ (-+-)	++++ (——)	++++ (+—)	++++ (+—)
756	C-H		++++	++++ (++-)	++++ (-++-)	++++ (+—)	++++ (+—)	++++ (+—)
1030	C-O			+++	++++ (-+++)	++++ (-++)	++++ (+—)	++++ (+—)
1493	C=C				++++	++++ (+—)	++++ (+—)	++++ (—)
1600	C=C					++++	++++ (+—)	++++ (+—)
1666	C=O						++++	++++ (-+-)
1744	O-C=O							++++

Note that 001FeH, 100FeR and 012FeC are short for hematite with {001}, {100} and {012} crystal facets, respectively.

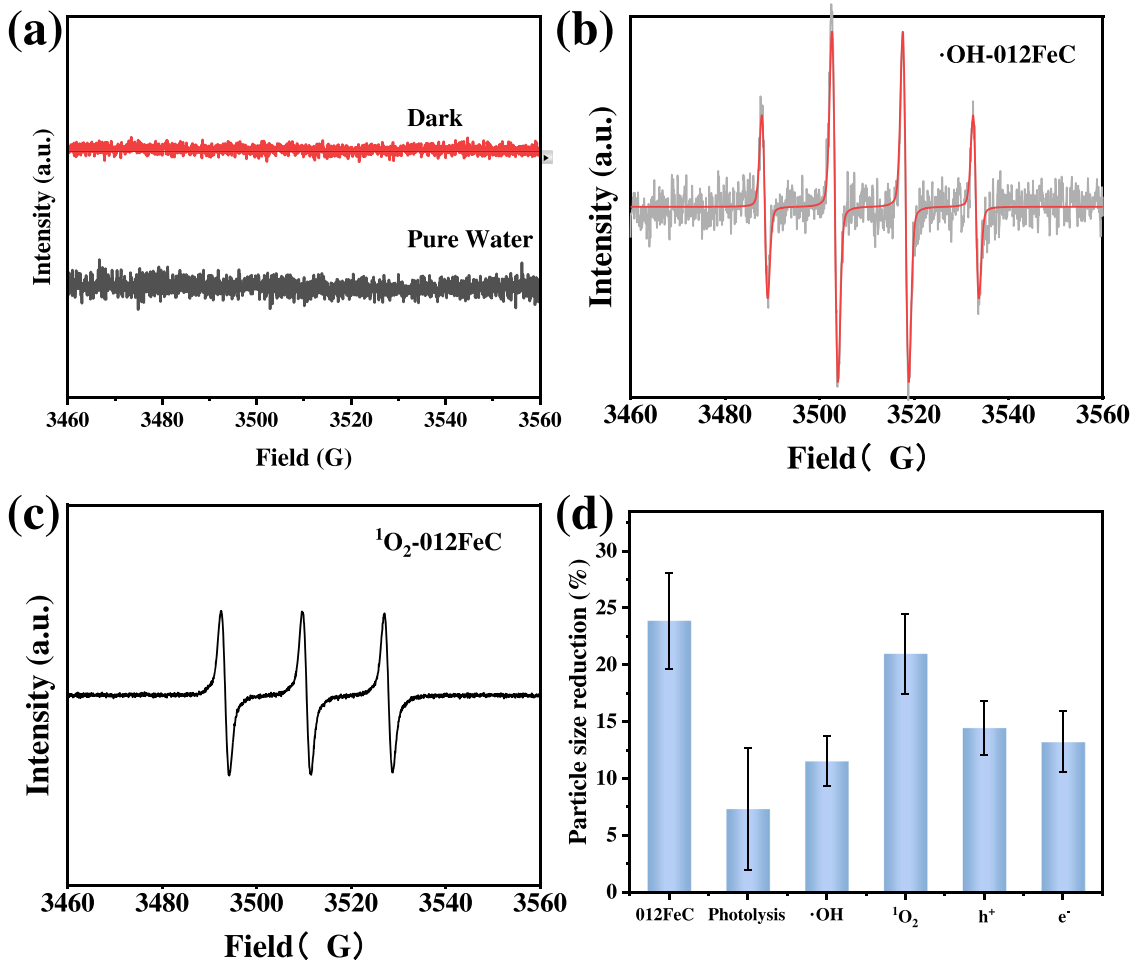

Fig. 5. Electron paramagnetic resonance (EPR) spectra of dark control and pure water (a), •OH (b) and $^1O_2$ (c) under irradiation and in the presence of hematite with {012} crystal facets (012FeC); the particle size reduction after quenching different reactive oxygen species in the presence of 012FeC (d).

4. Materials and methods

4.1. Materials

Ferric chloride ($FeCl_3$•$6H_2O$, 99.0%), sodium acetate (CH_3COONa, 99.0%), 1,2-diaminopropane ($C_3H_{10}N_2$, 99.0%), and ethanol (C_2H_5OH) were purchased from Shanghai Macklin Biochemical Co., Ltd. PS-MPs (diameter: ~200 μm; density: 1.05 g/cm^3) were purchased from Guangzhou Huayu Environmental Technology, Inc. (Guangzhou, China). Before the reaction, the PS-MPs were thoroughly washed with ultrapure water and filtered through a cotton filter (0.45 μm) to remove chemicals that may be adsorbed on the surface. The filtered samples were freeze-dried for 24 h and stored for further usage.

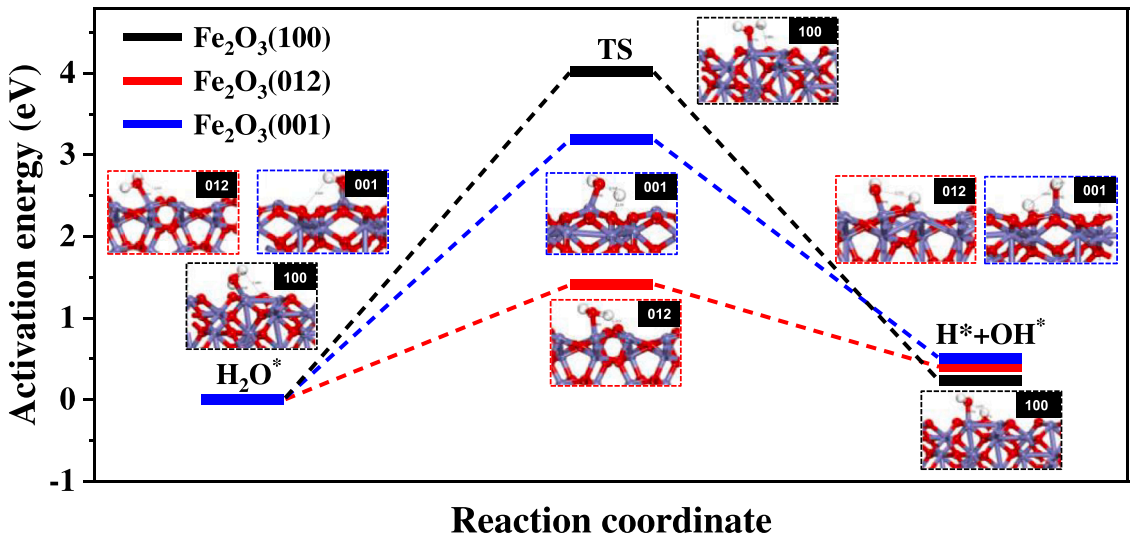

Fig. 6. The activation energy barrier of water oxidation to hydroxyl groups on hematite with different crystal facets exposed based on density functional theory (DFT) calculations.

4.2. Preparation of hematite {001}, {100} and {012}

For hematite {001} preparation, $FeCl_3$ (0.65 g) was added to a mixed solution of 40 mL ethanol and 2.8 mL pure water under a stirring rate of 500 r/min. After 0.5 h, 3.2 g of sodium acetate was added and stirred for 1 h. Subsequently, the mixed suspension was transferred into a 50 mL Teflon-lined stainless-steel autoclave and heated to 180 °C in an oven for 12 h.

For hematite {100} preparation, 4.05 g $FeCl_3 \bullet 6H_2O$ was added to 30 mL pure water and stirred for 0.5 h. Then, 30 mL 1,2-diaminopropane was added to the suspension and stirred for 0.5 h. Subsequently, the suspension was sealed in a 100 ml Teflon-lined stainless-steel autoclave and heated to 180 °C in an oven for 12 h.

For hematite {012} preparation, 1.092 g $FeCl_3 \bullet 6H_2O$ was added to a mixed solution of 40 mL H_2O and 10 mL ethanol under a stirring rate of 500 r/min. After 0.5 h, 3.2 g of sodium acetate was added and stirred for 1 h. Subsequently, the mixed suspension was transferred into a 50 mL Teflon-lined stainless-steel autoclave and heated to 180 °C in an oven for 12 h.

After the hydrothermal reaction, all the samples were washed using pure water and ethanol several times to remove impurities in the reaction solution. Subsequently, they were dried in an oven at 70 °C. Depending on the crystal facets of hematite, the morphologies of {001}, {100}, and {012} exhibited hexagonal nanosheets, nanorods, and nanocubes, respectively, based on the structural analysis below, which were named 001FeH, 100FeR, and 012FeC, respectively.

4.3. PS-MPs photoaging with hematite

The PS-MPs photoaging experiment was performed in a PCX-50C Discover multichannel photocatalytic reactor (Beijing Perfect Light Technology Co., Ltd., China). Each channel was equipped with a 50 mL sealed glass vial with a quartz bottom and a white LED (5 W) lamp as the light source to simulate sunlight irradiation (128 mW/cm^{-1}). Before the reaction, 30 mg PS-MPs and 50 mg fresh hematite samples were added to 30 mL ultrapure water. The MPs concentration in the experiment was higher than the environmental concentration in freshwater for manifesting the effect of photoaging (Lasee et al., 2017), as determined according to the previous studies (Bai et al., 2022; Ding et al., 2022). Ultrapure water was selected for excluding the influences of other environmental factors in the realistic freshwater. The mixed suspension was sonicated for 5 min and placed in each channel. Subsequently, the stirring rate was set at 500 r/min, and the light was turned on to initiate the reaction. The reaction temperature was controlled at 25 °C with a circulating water bath. After irradiation, PS-MPs were separated by a 10 μm filter. PS-MPs were then washed with pure water several times, freeze-dried, and stored in the dark for further analysis. The reaction solution during PS-MPs photoaging was filtered through prewashed Whatman GF/F filters (0.45 μm) to obtain plastic-derived DOM samples. In the control experiment, PS-MPs photoaging was conducted in pure water (without hematite addition), and PS-MPs were analyzed under dark conditions for comparison. The adsorption of hematite on PS-MPs was also determined under dark conditions, which was analyzed using an inductive coupled plasma emission spectrometer (ICP, ThermoFisher Scientific, iCAP 7000 SERIES). Each treatment was repeated three times.

4.4. Characterization of hematite

X-ray diffraction (XRD) patterns were obtained using a Bruker D8 Advance X-ray diffractometer with Cu-Kα radiation at a scanning rate of 5°/min. The N_2 adsorption-desorption isotherms were obtained at 77 K with a micromeritics ASAP 2010 instrument, and the specific surface area (S_{BET}), pore size (D_P), and pore volume (V_P) were calculated by applying the Brunauer–Emmett–Teller (BET) and Barrett–Joyner–Halenda (BJH) models. The morphologies and particle sizes of the samples were determined using field emission scanning electronic microscopy (FESEM; JEOL JSM-6380LV) and transmission electronic microscopy (TEM; Talos F200X G2, superX). The surface electronic states of the samples were investigated by X-ray photoelectron spectroscopy (XPS; ThermoFisher Scientific K-Alpha Nexsa using Al Kα radiation). UV–vis diffuse reflection spectra (DRS) were obtained on a Shimadzu UV-2450 spectrophotometer with $BaSO_4$ as a reference. The steady-state photoluminescence (PL) spectra were obtained using a Varian Cary-Eclipse 500 fluorometer at an excitation wavelength of 320 nm. Photocurrent spectra were obtained by an electrochemical analyzer (CHI760D Instruments) with a standard three-electrode system, where a 0.5 M Na_2SO_4 aqueous solution was used as the electrolyte, and the system was irradiated with a 300 W Xe lamp at intervals of 30 s. Electrochemical impedance spectra (EIS) were obtained under the open-circuit potential condition, with an amplitude of 10 mV and frequency span from 10 kHz to 0.01 Hz. The sample for the electrochemical experiment was prepared according to previously reported procedures (He et al., 2021).

4.5. Characterization of PS-MPs and DOM

Optical microscopy (Olympus CKX53, Japan) was applied to determine the particle size of PS-MPs, which was obtained by the average particle size of 50 MPs to avoid the personal error. The surface functional groups of PS-MPs before and after the reaction were explored by Fourier transform infrared spectroscopy (FTIR; Shimadzu IRTracer-100, Japan) in the range from 4000 to 400 cm^{-1}, and each spectrum adopted the average of 32 scans with 4 cm^{-1} resolution. The carbonyl index (CI) was calculated from the peak area of the carbonyl (1743 cm^{-1}) relative to the methylene (1452 cm^{-1}) in FTIR analysis (Dong et al., 2022). The surface alteration of the functional groups of PS-MPs was also confirmed using the X-ray photoelectron spectroscopy (XPS; ThermoFisher Scientific K-Alpha Nexsa using Al Kα radiation). Two-dimensional correlation spectroscopy (2D-COS) was employed in the analysis of PS-MPs with different reaction times. Synchronous and asynchronous spectra were obtained using 2D Shige software (Mao et al., 2020). The dissolved organic carbon (DOC) concentration of the leached DOM from PS-MPs was determined using a Total organic carbon (TOC) analyzer (Shimadzu, TOC-L, Japan). The aromaticity of released DOM was investigated by UV−vis absorption spectroscopy (Shimadzu, UV-3600 Plus, Japan), which was defined according to the absorbance at 254 nm divided by the DOC content of the sample (mg C/L, $SUVA_{254}$) (Wu et al., 2020).

4.6. ROS identification

The formation of ROS on different facets of hematite was determined by electron paramagnetic resonance (EPR) spectroscopy (Bruker EMX-plus, Germany) using 5,5-dimethyl-1-pyrroline N-oxide (DMPO; 50 mM) to capture •OH and $\bullet O_2^-$ and 2,2,6,6-Tetramethyl-4-piperidone (TEMP; 50 mM) to capture $^1O_2$ (Nguyen et al., 2022). The instrumental parameters were set as follows: center field = 3510 G; microwave frequency = 9.854 GHz; microwave power = 20 mW. The dark control experiment was conducted under the same conditions without light irradiation.

To evaluate the contribution of different radicals in the reaction, quenching experiments for different radicals were performed. The •OH, $^1O_2$, holes, and electrons during PS-MPs photoaging were quenched using tertiary butyl alcohol (TBA; 10 mM), furfuryl alcohol (FFA; 10 mM), ethylenediaminetetraacetic acid disodium salt (EDTA-2Na; 10 mM), and 2,3-dichloro-5,6-dicyano-1,4-benzoquinone (DDQ; 10 mM) as scavengers, respectively (Li et al., 2017; Ren et al., 2022; Wang et al., 2022). The particle size reduction of PS-MPs was used to assess the effect of diverse radicals on PS-MPs photoaging.

The •OH quantification was confirmed by the steady-state concentration ([•OH]ss) (Fig. S8), which was conducted through the terephthalic acid (TPA) probe method (Liu et al., 2022). Specifically, 0.5 mM TPA was dissolved in 30 mL 4 mM NaOH solution and filtered through a 0.7 μm filter (Whatman, GF/A). Then, 50 mg of hematite was added. During the reaction, TPA could combine with •OH to form hydroxy terephthalic acid (HTPA), which can be detected using a fluorescence spectrophotometer. The excitation and emission wavelengths were set at 315 nm and 425 nm, respectively (Xu et al., 2019). [•OH]ss was calculated as follows.

$$[\cdot OH] = f(0.01127FI - 0.26137)$$

Where f is the trapping factor, and f = 1.25; FI is fluorescence intensity; $[\cdot OH]_{ss}$ is the steady concentration of·OH (μM).

4.7. DFT calculations

Density functional theory (DFT) was applied to investigate the thermodynamic process of ROS generation on three hematite crystal surfaces. All three different reaction surfaces were built using an Fe_2O_3 unit cell using a vacuum region of 15 Å to separate the repeating slabs for these calculational models. DMol3 code was employed in the self-consistent periodic DFT calculations with the Grimme-06 (DFT-D2) method. Detailed information is provided in the supplementary material.

CRediT authorship contribution statement

Jiehong He: Conceptualization, Investigation, Data curation, Writing – original draft. **Lanfang Han:** Conceptualization, Investigation, Funding acquisition, Writing – review & editing. **Weiwei Ma:** Methodology, Investigation. **Chao Xu:** Writing – review & editing. **Elvis Genbo Xu:** Writing – review & editing. **Chuanxin Ma:** Writing – review & editing. **Baoshan Xing:** Supervision, Writing – review & editing. **Zhifeng Yang:** Funding acquisition, Supervision, Writing – review & editing.

Declaration of Competing Interest

The authors declare that they have no known competing financial interests or personal relationships that could have appeared to influence the work reported in this paper.

Data availability

Data will be made available on request.

Acknowledgments

This research was supported by the Program for Guangdong Introducing Innovative and Enterpreneurial Teams (2019ZT08L213), National Natural Science Foundation of China (42277203), the open competition program of top ten critical priorities of Agricultural Science and Technology Innovation for the 14th Five-Year Plan of Guangdong Province (2022SDZG08), and Guangdong Basic and Applied Basic Research Foundation (2022A1515111112). E.G.X. thank the support of the Department of Biology, University of Southern Denmark, and Danmarks Frie Forskningsfond.

Supplementary materials

Supplementary material associated with this article can be found, in the online version, at doi:10.1016/j.wroa.2023.100185.

References

Asif, A.H., Wang, S., Sun, H., 2021. Hematite-based nanomaterials for photocatalytic degradation of pharmaceuticals and personal care products (PPCPs): a short review. Curr. Opin. Green Sust. 28, 100447.
Bai, X., Ma, W., Zhang, Q., Zhang, L., Zhong, S., Shu, X., 2022. Photon-induced redox chemistry on pyrite promotes photoaging of polystyrene microplastics. Sci. Total Environ. 829, 154441.
Baltrusaitis, J., Cwiertny, D.M., Grassian, V.H., 2007. Adsorption of sulfur dioxide on hematite and goethite particle surfaces. Phys. Chem. Chem. Phys. 9 (41), 5542–5554.
Bardestani, R., Patience, G.S., Kaliaguine, S., 2019. Experimental methods in chemical engineering: specific surface area and pore size distribution measurements-BET, BJH, and DFT. Can. J. Chem. Eng. 97 (11), 2781–2791.
Chen, L., Wang, X., Rao, Z., Tang, Z., Wang, Y., Shi, G., Lu, G., Xie, X., Chen, D., Sun, J., 2021. *In-situ* synthesis of Z-Scheme MIL-100(Fe)/α-Fe_2O_3 heterojunction for enhanced adsorption and visible-light photocatalytic oxidation of O-xylene. Chem. Eng. J. 416, 129112.
Cornell, R.M., Schwertmann, U., 2003. The Iron Oxides: Structure, Properties, Reactions, Occurrences, and Uses. Wiley-vch Weinheim.
Ding, L., Guo, X., Du, S., Cui, F., Zhang, Y., Liu, P., Ouyang, Z., Jia, H., Zhu, L., 2022. Insight into the photodegradation of microplastics boosted by iron (hydr)oxides. Environ. Sci. Technol. 56 (24), 17785–17794.
Ding, L., Mao, R., Ma, S., Guo, X., Zhu, L., 2020. High temperature depended on the ageing mechanism of microplastics under different environmental conditions and its effect on the distribution of organic pollutants. Water Res. 174, 115634.

Dong, S., Yan, X., Yue, Y., Li, W., Luo, W., Wang, Y., Sun, J., Li, Y., Liu, M., Fan, M., 2022. H_2O_2 concentration influenced the photoaging mechanism and kinetics of polystyrene microplastic under UV irradiation: direct and indirect photolysis. J. Clean. Prod. 380, 135046.
Duan, J., Li, Y., Gao, J., Cao, R., Shang, E., Zhang, W., 2022. ROS-mediated photoaging pathways of nano- and micro-plastic particles under UV irradiation. Water Res. 216, 118320.
He, J., Lyu, P., Jiang, B., Chang, S., Du, H., Zhu, J., Li, H., 2021. A novel amorphous alloy photocatalyst (NiB/In_2O_3) composite for sunlight-induced CO_2 hydrogenation to HCOOH. Appl. Catal. B 298, 120603.
Hu, D., Zhang, Y., Shen, M., 2020. Investigation on microplastic pollution of Dongting Lake and its affiliated rivers. Mar. Pollut. Bull. 160, 111555.
Hussain, D., Siddiqui, M.F., Shirazi, Z., Khan, T.A., 2022. Evaluation of adsorptive and photocatalytic degradation properties of $FeWO_4$/polypyrrole nanocomposite for rose Bengal and alizarin red S from liquid phase: modeling of adsorption isotherms and kinetics data. Environ. Prog. Sustain. 41 (4), e13822.
Jin, P., Song, J., Wang, X.C., Jin, X., 2018. Two-dimensional correlation spectroscopic analysis on the interaction between humic acids and aluminum coagulant. J. Environ. Sci. 64, 181–189.
Lasee, S., Mauricio, J., Thompson, W.A., Karnjanapiboonwong, A., Kasumba, J., Subbiah, S., Morse, A.N., Anderson, T.A., 2017. Microplastics in a freshwater environment receiving treated wastewater effluent. Integr. Environ. Assess. Manag. 13 (3), 528–532.
Li, R., Che, R., Liu, Q., Su, S., Li, Z., Zhang, H., Liu, J., Liu, L., Wang, J., 2017. Hierarchically structured layered-double-hydroxides derived by ZIF-67 for uranium recovery from simulated seawater. J. Hazard. Mater. 338, 167–176.
Lithner, D., Larsson, Å., Dave, G., 2011. Environmental and health hazard ranking and assessment of plastic polymers based on chemical composition. Sci. Total Environ. 409 (18), 3309–3324.
Liu, J., Inoué, S., Zhu, R., He, H., Hochella, M.F., 2021. Facet-specific oxidation of Mn(II) and heterogeneous growth of manganese (oxyhydr)oxides on hematite nanoparticles. Geochim. Cosmochim. Acta 307, 151–167.
Liu, P., Qian, L., Wang, H., Zhan, X., Lu, K., Gu, C., Gao, S., 2019. New insights into the aging behavior of microplastics accelerated by advanced oxidation processes. Environ. Sci. Technol. 53 (7), 3579–3588.
Liu, Z., Lv, Y., Wang, Y., Wang, S., Odebiyi, O.S., Liu, B., Zhang, Y., Du, H., 2022. Oxidative leaching of V-Cr–bearing reducing slag *via* a Cr(III) induced Fenton-like reaction in concentrated alkaline solutions. J. Hazard. Mater. 439, 129495.
Luo, L., Wang, Z., Xiang, X., Yan, D., Ye, J., 2020. Selective activation of benzyl alcohol coupled with photoelectrochemical water oxidation *via* a radical relay strategy. ACS Catal. 10 (9), 4906–4913.
Lv, B., Liu, Z., Tian, H., Xu, Y., Wu, D., Sun, Y., 2010. Single-crystalline dodecahedral and octodecahedral α-Fe_2O_3 particles synthesized by a fluoride anion-assisted hydrothermal method. Adv. Funct. Mater. 20 (22), 3987–3996.
Lv, J., Miao, Y., Huang, Z., Han, R., Zhang, S., 2018. Facet-mediated adsorption and molecular fractionation of humic substances on hematite surfaces. Environ. Sci. Technol. 52 (20), 11660–11669.
Ma, D., Wu, J., Yang, P., Zhu, M., 2020. Coupled manganese redox cycling and organic carbon degradation on mineral surfaces. Environ. Sci. Technol. 54 (14), 8801–8810.
Mao, R., Lang, M., Yu, X., Wu, R., Yang, X., Guo, X., 2020. Aging mechanism of microplastics with UV irradiation and its effects on the adsorption of heavy metals. J. Hazard. Mater. 393, 122515.
Minor, E.C., Lin, R., Burrows, A., Cooney, E.M., Grosshuesch, S., Lafrancois, B., 2020. An analysis of microlitter and microplastics from Lake Superior beach sand and surface-water. Sci. Total Environ. 744, 140824.
Nguyen, B., Claveau-Mallet, D., Hernandez, L.M., Xu, E.G., Farner, J.M., Tufenkji, N., 2019. Separation and analysis of microplastics and nanoplastics in complex environmental samples. Acc. Chem. Res. 52 (4), 858–866.
Nguyen, T.T., Kim, D.G., Ko, S.O., 2022. Changes in the catalytic activity of oxygen-doped graphitic carbon nitride for the repeated degradation of oxytetracycline. Chemosphere 307, 135870.
Novotna, K., Cermakova, L., Pivokonska, L., Cajthaml, T., Pivokonsky, M., 2019. Microplastics in drinking water treatment-Current knowledge and research needs. Sci. Total Environ. 667, 730–740.
Parashar, N., Hait, S., 2022. Occurrence and removal of microplastics in a hybrid growth sewage treatment plant from Bihar, India: a preliminary study. J. Clean. Prod. 376, 134295.
Qiu, X., Ding, L., Zhang, C., Ouyang, Z., Jia, H., Guo, X., Zhu, L., 2022. Exposed facets mediated interaction of polystyrene nanoplastics (PSNPs) with iron oxides nanocrystal. J. Hazard. Mater. 435, 128994.
Ren, Y., Chen, Y., Li, Q., Li, H., Bian, Z., 2022. Microwave-assisted photocatalytic degradation of organic pollutants *via* CNTs/TiO_2. Catalysts 12 (9), 940.
Shen, S., Lindley, S.A., Chen, X., Zhang, J.Z., 2016. Hematite heterostructures for photoelectrochemical water splitting: rational materials design and charge carrier dynamics. Energy Environ. Sci. 9 (9), 2744–2775.
Su, L., Xue, Y., Li, L., Yang, D., Kolandhasamy, P., Li, D., Shi, H., 2016. Microplastics in Taihu Lake. China. Environ. Pollut. 216, 711–719.
Tang, Y., Liu, Y., Chen, Y., Zhang, W., Zhao, J., He, S., Yang, C., Zhang, T., Tang, C., Zhang, C., Yang, Z., 2021. A review: research progress on microplastic pollutants in aquatic environments. Sci. Total Environ. 766, 142572.
Wang, A., Chen, W., Geng, N., Lan, X., Liu, M., Wu, X., 2022. Novel electrochemical preparation of N-doped TiO_2/graphene for enhanced stability and photocatalysis degradation of humic acid. Sustainability 14 (17), 10614.
Wu, D., Ren, C., Jiang, L., Li, Q., Zhang, W., Wu, C., 2020. Characteristic of dissolved organic matter polar fractions with variable sources by spectrum technologies: chemical properties and interaction with phenoxy herbicide. Sci. Total Environ. 724, 138262.
Wu, X., Liu, P., Gong, Z., Wang, H., Huang, H., Shi, Y., Zhao, X., Gao, S., 2021. Humic acid and fulvic acid hinder long-term weathering of microplastics in lake water. Environ. Sci. Technol. 55 (23), 15810–15820.
Xu, L., Li, H., Mitch, W.A., Tao, S., Zhu, D., 2019. Enhanced phototransformation of tetracycline at smectite clay surfaces under simulated sunlight *via* a lewis-base catalyzed alkalization mechanism. Environ. Sci. Technol. 53 (2), 710–718.
Yanina Svetlana, V., Rosso Kevin, M., 2008. Linked reactivity at mineral-water interfaces through bulk crystal conduction. Science 320 (5873), 218–222.
Yu, W., Zhao, L., Chen, F., Zhang, H., Guo, L., 2019. Surface bridge hydroxyl-mediated promotion of reactive oxygen species in different particle size TiO_2 suspensions. J. Phys. Chem. Lett. 10 (11), 3024–3028.
Yuan, W., Liu, X., Wang, W., Di, M., Wang, J., 2019. Microplastic abundance, distribution and composition in water, sediments, and wild fish from Poyang Lake. China. Ecotoxicol. Environ. Saf. 170, 180–187.
Zhang, X., Xia, M., Zhao, J., Cao, Z., Zou, W., Zhou, Q., 2022a. Photoaging enhanced the adverse effects of polyamide microplastics on the growth, intestinal health, and lipid absorption in developing zebrafish. Environ. Int. 158, 106922.
Zhang, Y., Cheng, F., Zhang, T., Li, C., Qu, J., Chen, J., Peijnenburg, W.J.G.M., 2022b. Dissolved organic matter enhanced the aggregation and oxidation of nanoplastics under simulated sunlight irradiation in water. Environ. Sci. Technol. 56 (5), 3085–3095.
Zhou, X., Lan, J., Liu, G., Deng, K., Yang, Y., Nie, G., Yu, J., Zhi, L., 2012. Facet-mediated photodegradation of organic dye over hematite architectures by visible light. Angew. Chem. Int. Edit. 51 (1), 178–182.
Zhou, Z., Huang, G., Xiong, Y., Zhou, M., Zhang, S., Tang, C.Y., Meng, F., 2017. Unveiling the susceptibility of functional groups of poly(ether sulfone)/polyvinylpyrrolidone membranes to NaOCl: a two-dimensional correlation spectroscopic study. Environ. Sci. Technol. 51 (24), 14342–14351.
Zhu, H., Gong, L., Chen, Z., Hu, Y., Li, Z., 2020. Al cluster oxide modified a hematite/P3HT ternary Z-scheme photocatalyst with excellent photocatalytic performance: a discussion of the mechanism. J. Hazard. Mater. 391, 122252.
Zhu, K., Sun, Y., Jiang, W., Zhang, C., Dai, Y., Liu, Z., Wang, T., Guo, X., Jia, H., 2022. Inorganic anions influenced the photoaging kinetics and mechanism of polystyrene microplastic under the simulated sunlight: role of reactive radical species. Water Res. 216, 118294.